SANDIA REPORT
SAND2007-7377
Printed January 2008

Integrated NEMS and Optoelectronics for Sensor Applications

David A. Czaplewski, Uma Krishnamoorthy, Murat Okandan, Roy H. Olsson III, Kenneth A. Peterson, Darwin K. Serkland, Dustin W. Carr, Gregory R. Bogart, and Mial E. Warren

Prepared by
Sandia National Laboratories
Albuquerque, New Mexico 87185

Sandia is a multiprogram laboratory operated by Sandia Corporation, a Lockheed Martin Company, for the United States Department of Energy's National Nuclear Security Administration under contract DE-AC04-94AL85000.

Issued by Sandia National Laboratories, operated for the United States Department of Energy by Sandia Corporation.

SAND 2007-7377
Unclassified Unlimited Release
Printed January 2008

Integrated NEMS and Optoelectronics for Sensor Applications (LDRD Project 79761)

David A. Czaplewski, Uma Krishnamoorthy, Murat Okandan, Roy H. Olsson III
MEMS Device Technologies and Reliability Physics, Dept. 1749

Kenneth A. Peterson
Thin film, vacuum, and packaging, Dept. 2452

Darwin K. Serkland
RF and Optoelectronics, Dept. 1742

Mial E. Warren
Microsystems partnerships, Dept. 5624

Sandia National Laboratories
P.O.Box 5800
Albuquerque, NM 87185

Dustin W. Carr, Gregory R. Bogart
Symphony Acoustics,
103 Rio Rancho Drive, Suite B-4
Rio Rancho, NM 87124

Abstract

This work utilized advanced engineering in several fields to find solutions to the challenges presented by the integration of MEMS/NEMS with optoelectronics to realize a compact sensor system, comprised of a microfabricated sensor, VCSEL, and photodiode. By utilizing microfabrication techniques in the realization of the MEMS/NEMS component, the VCSEL and the photodiode, the system would be small in size and require less power than a macro-sized component. The work focused on two technologies, accelerometers and microphones, leveraged from other LDRD programs. The first technology was the nano-g accelerometer using a nanophotonic motion detection system (67023). This accelerometer had measured sensitivity of approximately 10 nano-g. The Integrated NEMS and optoelectronics LDRD supported the nano-g accelerometer LDRD by providing advanced designs for the accelerometers, packaging, and a detection scheme to encapsulate the accelerometer, furthering the testing

capabilities beyond bench-top tests. A fully packaged and tested die was never realized, but significant packaging issues were addressed and many resolved. The second technology supported by this work was the ultrasensitive directional microphone arrays for military operations in urban terrain and future combat systems (93518). This application utilized a diffraction-based sensing technique with different optical component placement and a different detection scheme from the nano-g accelerometer. The Integrated NEMS LDRD supported the microphone array LDRD by providing custom designs, VCSELs, and measurement techniques to accelerometers that were fabricated from the same operational principles as the microphones, but contain proof masses for acceleration transduction. These devices were packaged at the end of the work.

Acknowledgements

The authors would like to acknowledge Mike Baker for help with design and simulation, Ken Pohl for circuit layout and assembly, and Neil Hall for experimental measurements. We would like to acknowledge the staff of the Sandia Microsystems Development Laboratory (MDL) and Compound Semiconductor Research Laboratory (CSRL) who contributed to the fabrication of these devices. This work was supported in full by a Laboratory Directed Research and Development project (79761) at Sandia National Labs. Sandia is a multiprogram laboratory operated by Sandia Corporation, a Lockheed Martin Company, for the United States Department of Energy's National Nuclear Security Administration under contract DE-AC04-94AL85000.

CONTENTS

1 INTRODUCTION

This project takes on the challenging issues involved in the integration of NEMS/MEMS and optoelectronics to make compact sensor systems, with the primary goal being a very small accelerometer with nano-g sensitivity. Besides the clear benefits of size reduction in a single sensor system, another motivation for pursuing this miniaturization is to more easily fabricate sensor arrays. Multiple sensor elements can be used for noise reduction and system robustness in inertial sensing. In many ways this research is foundational in nature and will feed into many related programs that are growing from optical based sensing solutions. The focus in this work is on understanding methods of integration, as well as the physical challenges that are involved in closely coupling active optical components, such as lasers and photodiodes, with moving structures that can be used in physical sensors.

The ultimate goal of this project was to enable a measurement, currently requiring an optical bench top setup, to be performed in a portable system as small as possible. In order to achieve this, the optical measurements requiring large gas lasers, mirrors, and stand-alone photodiodes were miniaturized into integrated components. The optical components can be miniaturized to sub 1 mm^3 structures. Additionally, this approach required the design, fabrication and release of novel micro-devices that took advantage of the close proximity of the optical components to measure acceleration. The optical and mechanical components were combined using several packaging techniques. Finally, noise analysis was performed to determine the minimum sensitivities for the assembled devices using circuitry optimized for noise cancellation and reduction. The following report describes the efforts and achievements toward the above-mentioned focus areas.

2 OPTICAL MINIATURIZATION

The miniaturization process focused on two aspects, optical and mechanical miniaturization. This section will focus on the results of making the optical measurements smaller. Discussion of mechanical miniaturization will occur in subsequent chapters.

Optical tables provide many convenient features that allow for adaptable optical measurements, such as periodic placement of components, vibration isolation, co-planar setup, and many others. Unfortunately, their large size (typically m^2 areas) and weight (>100 kg) make them impractical for portable measurements for sensing applications. In spite of these drawbacks, most advance concept sensors still require the measurements to be made on optical tables. The goal of this work is to eliminate the need to make measurements using optical systems mounted on optical tables. In order to measure accelerations on the order of nano-g ($\sim 10^{-8}$ m/s^2) in past sensing systems, large optical systems were required (Fig. 1).

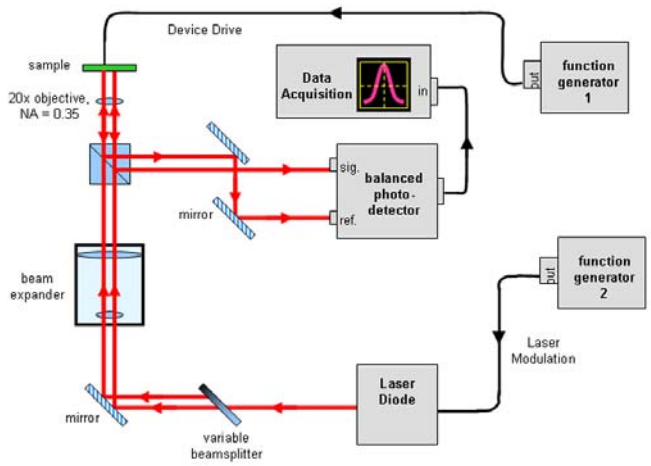

Figure 1 Schematic of the bench-top experimental setup required to measure nano-g accelerations.

The focus of the work was to reduce these components to something that could be transported between locations without a forklift.

The first effort focused on miniaturization through the use of macro-size components. These would be assembled to achieve a smaller version of the optical table. The second effort focused on miniaturization through the use of commercially available systems, such as CD-ROM read heads. The final and main effort of the project used micro-sized components (VCSELs and PDs) and took advantage of the dimensions of these components and their relative placements to achieve portable sensor systems.

2.1 Macro components

The first effort focused on using macro-size components to achieve miniaturization of the optical measurement setup. Using macro-size components such as beam splitters, lasers, lenses, and mirrors (Fig. 2a), a design was created and analyzed (Fig 2b).

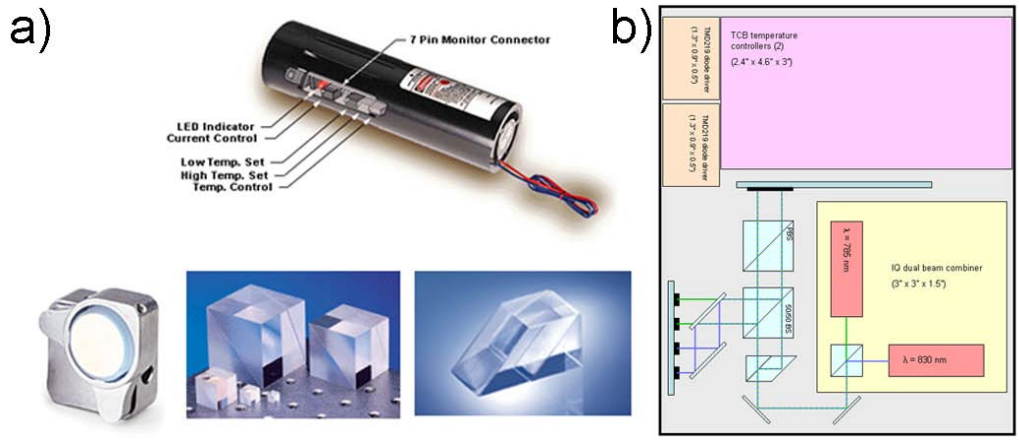

Figure 2 a) Macro-scale components used to construct first miniature measurement setup (b).Schematic of the completed system showing the placement and relative size of all the components.

The two lasers were designed to be solid state lasers. These lasers are currently used in the telecommunications industry and are readily available. The beam splitters and mirrors are available commercially. These components can be mounted to a rail system, which would provide optical alignment for the components. Specific antireflective coatings are available through these same commercial vendors. These optical components would allow precision placement and alignment of components. However, the end size of ~ 3" x 6" x 6" was too large for some of the interested groups. These components would not be shock resistant, and would require significant power to maintain operation. Additionally, the weight of the assembled components was too large for prospective needs.

2.2 Commercial components

The second effort focused on the integration of commercial available components used in CD and DVD players to read/write purposes. A schematic of the design concept can be seen in figure 3.

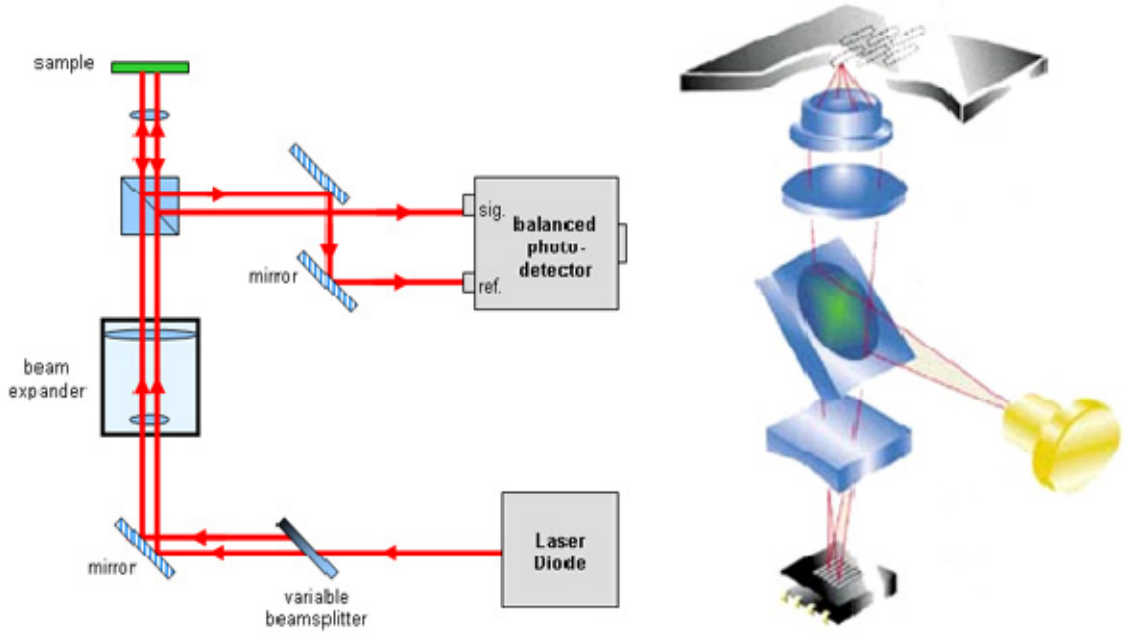

Figure 3 Schematic showing the reduction of the table top experiment into a commercially available optical measurement system used in CD-ROM read/write heads.

This option was feasible from cost and availability concerns. However, the layout of the components would be different in our operation. This would require manufacturing changes. The quantity to be desired by prospective users was too small to be of interest to commercial manufacturers of these components.

2.3 Micro-components

The majority of the effort focused on miniaturizing the entire system using microfabricated components. The table top laser would be replaced by a VCSEL. The mirrors would not be needed because of the close proximity that the individual parts were assembled. The photodiodes could be designed in-house for the specific geometries required. The accelerometers would be modified from other LDRD programs, specifically, a nano-g accelerometer (67023) and a diffraction based accelerometer (93518). The discussion of contributions made to these microsystems will be discussed in detail later in the report.

2.3.1 *VCSEL Measurements*

Laser diode noise is typically quantified as relative intensity noise (RIN), which is conveniently expressed in terms of measured detector photocurrent as

$$RIN = \frac{i_n^2}{I_{DC}^2},$$

where i_n is the photocurrent noise density (A/√Hz) and I_{DC} is the DC photocurrent. For a shot-noise limited laser the measured noise is $i_n^2 = 2qI_{DC}$, so $RIN = 2q / I_{DC}$. As a specific example, a shot-noise limited laser that produces a photocurrent of 1mA yields a RIN of -155 dB/Hz. Unfortunately, semiconductor lasers typically exhibit excess noise above the shot-noise level. Moreover, VCSELs are known to exhibit 1/f noise, which makes high-sensitivity measurements at audio and lower frequencies especially challenging. While the Hobbs differential detector circuit can cancel a significant amount of excess noise, the noise reduction is typically limited to about 20 to 30 dB. Hence, it is desirable to minimize the intrinsic noise from the VCSEL to the point where the Hobbs circuit can cancel the remaining excess noise and thus approach the shot-noise limit.

We measured the low-frequency RIN of two candidate single-mode 850-nm VCSELs: a Sandia VCSEL (wafer EMC8166) and a commercial VCSEL from Avalon Photonics (AVAP-850SM). In order to measure low levels of RIN, it is essential to use a photodetector that contributes minimal noise. For our measurements, we used a New Focus model 2001 amplified photodetector, which has a responsivity of $\Re$=0.635A/W at 850 nm and a transimpedance gain of R=5.6 kOhm (at Gain=10). Thus, an optical input power P=1.13 mW produced an output voltage $V_{NF}=\Re RP$= 4.0 V. The output of the photodetector was measured with an FFT Spectrum Analyzer (SRS model SR785) to obtain the noise spectral density, as shown in Figure 4. For these measurements, both lasers were operated at an output power level of P = 1.13 mW. The Sandia VCSEL was more efficient, requiring only 3.0mA of drive current to achieve 1.13 mW of output, as shown in Figure 5. The Avalon VCSEL exhibited a high threshold current of 4.1 mA, as shown in Figure 5, and was biased at 7.5 mA to achieve an output of 1.13 mW. Both CSELs exhibited a low 1/f corner frequency of 2 kHz. Because several Avalon VCSELs were available and because they exhibited 5 dB lower noise at 10 Hz, they were chosen for use in the subsequent experiments.

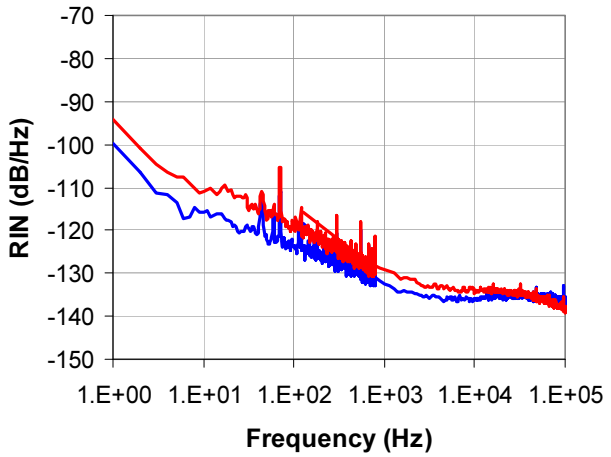

Figure 4 Measured low-frequency relative intensity noise (RIN) of two single-mode 850-nm VCSELs: (red) Sandia EMC8166-A_357_V23 and (blue) Avalon AVAP-850SM_42_124.

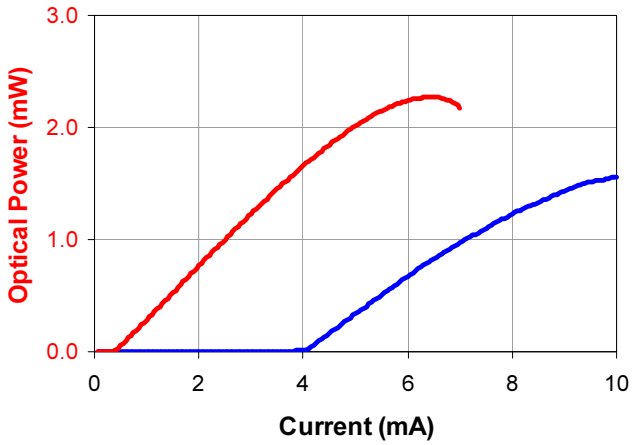

Figure 5 Measured light versus current curves for the two lasers of Fig. yy1: (red) Sandia EMC8166-A_357_V23 and (blue) Avalon AVAP-850SM_42_124.

Another important VCSEL characteristic to determine was the beam divergence angle, since the various diffraction orders must be sufficiently separated so they can be detected with three separate photodiodes. Figure 6 shows the measured beam divergence (half angle) from the Avalon single-mode VCSEL AVAP-850SM_42_116, which has a numerical aperture of 0.144. This is smaller than the beam divergence angle of the Sandia VCSELs. We believe that the Avalon VCSEL uses the top metal to define the beam aperture, which helps minimize beam divergence but at the expense of a relatively high threshold current.

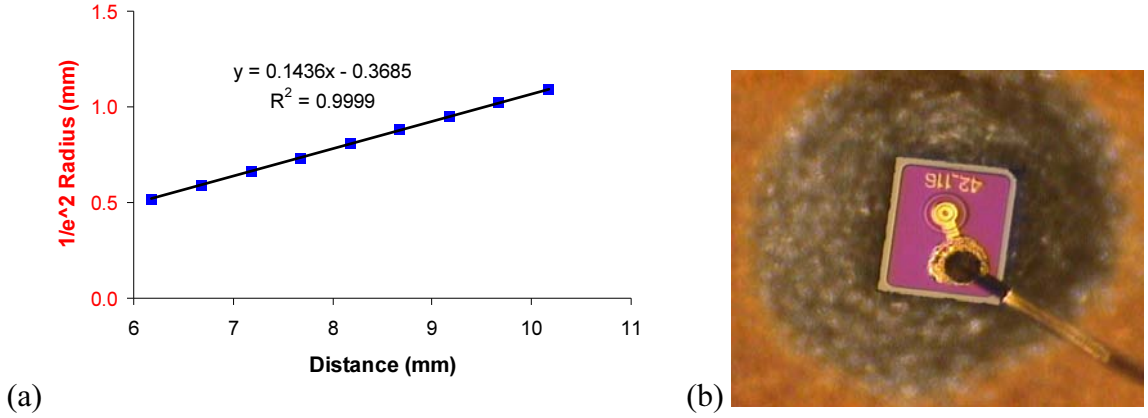

Figure 6 (a) Measured optical beam divergence (half angle) of Avalon VCSEL AVAP-850SM_42_116. (b) Photograph of the Avalon VCSEL mounted on a TO-39 header.

2.3.2 *Custom Silicon Photodiodes*

Two wafers of custom silicon photodiodes were designed and fabricated to produce small (250 µm by 500 µm) chips that could be positioned near enough to each other to separately capture beams from the three central diffraction orders: -1, 0, +1. The photodiode wafer was thinned to 150 µm so that the chips would be slightly less thick (150 µm) than wide (250 µm). Four types of photodiode chips were designed to meet a variety of potential applications. Figure 7 shows the four chip design types, labeled **A**, **B**, **C**, **D**. All chips have blanket back side metal of Ti/Pt/Au available as a cathode connection, and the top side metal pads (anode and optional cathode) are also Ti/Pt/Au. The active photodiode area is anti-reflection coated at 850 nm, with a single quarter-wave layer. Photodiode chip type **A** provides the largest active area, measuring 200 µm by 300 µm, and a single top-side anode connection. Photodiode chip types **B**, **C**, and **D** provide both anode and cathode pads on the top side of the chip, and active areas measuring 200 µm, 100 µm, and 50 µm, respectively, by 200 µm.

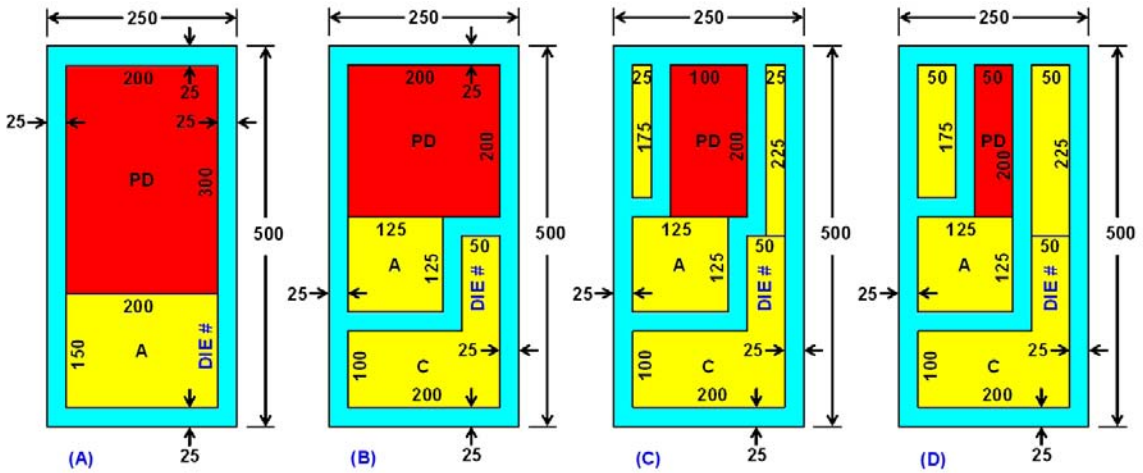

Figure 7 Four photodiode chip design types: A, B, C, D. The active photodiode area is shown in red, and the top-side metal pads are shown in yellow. The dimensions are indicated in microns. Top side metal bond pads are labeled "A" for anode and "C" for cathode.

The photodiodes were fabricated from 4-inch-diameter silicon wafers. The "Silicon2" mask set was designed with a repeating until cell, shown in Figure 8, which consists of a single row of 10 photodiode chips, numbered 0 to 9. Chips 0, 1, 2, 3 are type **A**; chips 4,5,6 are type **B**; chips 7,8 are type **C**; and chip 9 is type **D**. The chips are designed to measure 250 μm by 500 μm, and they are arranged on a pitch of 13 mil (330.2 μm) by 23 mil (584.2 μm) so they can be diced on a saw that steps in mil units and has a kerf width of approximately 80 μm.

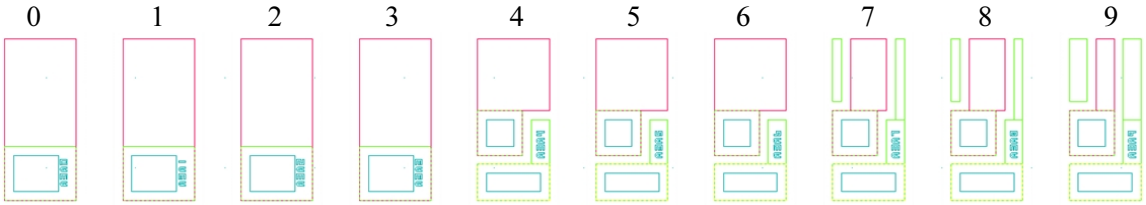

Figure 8 Unit cell of "Silicon2" mask set, containing 10 photodiode chips, numbered 0 to 9.

Each chip was fabricated with a 4-digit serial number of format RRCC that designates the row RR (A0, A1, … , A9, B0, B1, …, Z9) and column CC. According to this serial number format, the last digit is the chip number within each unit cell, and therefore corresponds to the chip design type. Unfortunately, the as-fabricated resolution was not sufficient to resolve the 25 μm tall digits in the serial numbers. However, we can reconstruct the serial number sequence by inspecting the entire wafer and noting that certain alpha-numeric characters usually produce a blank (I, 1), others produce only tiny (10 μm) dots (J, L, 7), while the remaining characters yield a full-size (20 μm) dot. Pictures of four fabricated chips from part OD-1737 wafer 116-2A are shown in Figure 9.

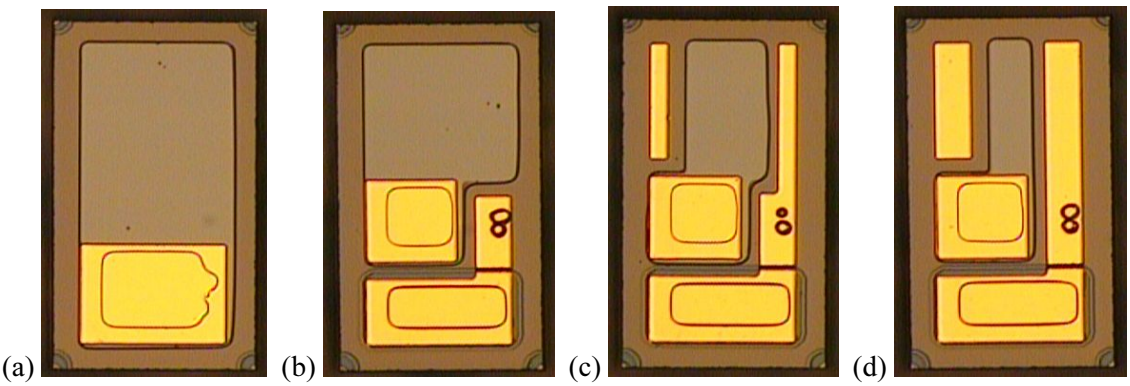

Figure 9 Microscope photographs of all four chip types. The die numbers are (a) I1N1, (b) I1M4, (c) I1M7, (d) I1M9. In the die number regions, the characters I and 1 appear blank and the character 7 appears as a smaller dot relative to the other characters.

Figure 10(a) shows the measured dark current versus reverse bias voltage of die number 14N0 (type A photodiode) of part OD-1737 wafer 116-2A. The dark current was 47pA at a reverse bias voltage of 2V. Figure 10(b) shows the actual photodiode chip on a probe station, immediately after the measurements were taken.

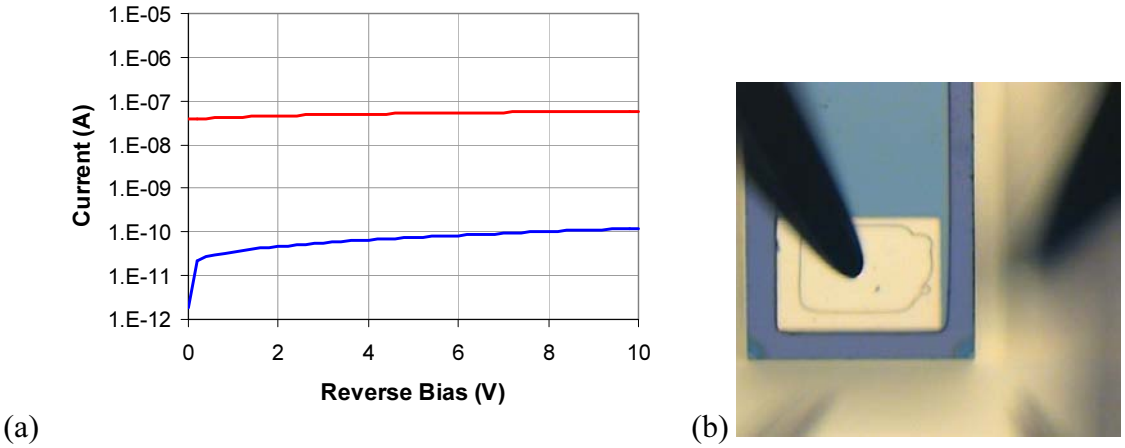

(a) (b)

Figure 10 (a) Dark current (blue) and white-light-illuminated current (red) from photodiode die number I4N0 (type A) of part OD-1737 wafer 116-2A. (b) Picture of the measured chip, sitting on a gold platen that electrically connects the (back side) cathode to the right-hand probe (out of focus).

3 ACCELEROMETERS

Two main microsystem technologies were explored to produce the highest sensitivity accelerometers. These technologies were leveraged from other LDRD programs: the nanophotonic motion detection system LDRD (67023) and the ultrasensitive directional microphone arrays for military operations in urban terrain and future combat systems (93518). This work complemented the nanophotonic gratings and worked to incorporate a proof mass into the fabrication process. The nano-photonics gratings operated on quantum tunnel principles, similar to optical band-gap designs. The

acceleration of the proof mass would displace a sub-wavelength optical grating with respect to a second grating in near proximity. The displacements of the gratings relative to each other would change the effective index of the structure and produce changes in light transmission or reflection from the structure. Additionally, this work complemented the microphone array, which was adapted to include a proof mass for acceleration transduction. The microphone-based accelerometer operated on Frauhofer diffraction principals. Acceleration of the proof mass would change the distance between a reflective membrane and an optical grating. The movement would change the optical pathlengths for constructive and destructive interference. The changes in pathlength would result in variations in intensity of the diffracted light from the grating. A summary of these efforts is listed below.

3.1 Nanophotonic gratings

Part of this LDRD supported the work to create an accelerometer from nanophotonic gratings. This effort focused on the incorporation of a proof mass to the gratings. The gratings themselves were fabricated from a modified SUMMiT V™ process flow. The operation principles of the nanophotonic grating performance can be found in the SAND report for the LDRD. To summarize, two gratings are fabricated to lie on top of each other with a small gap separating the two. The gratings have sub-wavelength dimensions and spacing and thus create a local effective index of refraction for that region of space. The index varies as a function of the relative placement of one grating to the other. During an acceleration event, the gratings move relative to each other, modulating the effective index of the structures. This changes the intensity of the reflected and transmitted light. The light typically arrives at normal incident angle on the grating. The reflected intensity is monitored to determine the relative displacement of the gratings, which resulted from accelerations applied to the device. In addition to incorporating a proof mass, several supported activities are also summarized in this report. A brief description of these activities will be discussed here.

In order to increase the sensitivity of the grating structure to accelerations, proof masses were designed into fabrication process. Two different processes were attempted before a more reproducible solution was incorporated. The first process was to deposit an epitaxial polysilicon layer onto the devices. This epi-poly layer would provide the added mass. The layer was deposited on structures connected to the sub-wavelength gratings. Unfortunately, the layer was difficult to etch using a deep reactive ion etch. The masking layer was not adequate to clear out all necessary areas. This process was not repeated because capabilities were developed to incorporate a higher density material into the processing. The second process involved electroplating gold onto the surface of the structure. Gold has a density of nearly 9 times that of polysilicon. The plating was successful but the process was determined to be too difficult and not reproducible enough to rely on for device fabrication. The effort turned toward incorporating the mass with the grating using the silicon substrate. The summary of the fabrication steps can be found in the nanophotonics SAND report.

Upon completion of the design and modeling, devices were fabricated. Basic layout of the mass integrated nanoG accelerometer device is shown in Figure 11a. A large mass is suspended by relatively weak mass springs that are attached to a suspended gimbal for improved thermal isolation.

Prior to this integration, we discovered that these nanograting-based devices were not robust enough to withstand standard handling, resulting in extremely low yield. We discovered two failure modes for the devices:

a. Grating membrane failure (Figure 11b) and
b. Mechanical spring (gimbal/mass springs) failure

Gratings and springs break when devices go through post-processing after the DRIE (Deep Reactive Ion Etch) that defines the mass, gimbal and springs. The point of failure for the grating membrane followed the lines of the underlying mass – possibly from direct impact during standard handling. The mechanical springs (both gimbal and mass) were susceptible to breakage during handling also. Typically, the membrane gratings failed before the springs. The following steps were identified as especially damaging to the devices (low yield):

1. Picking up the unreleased device chips from the dicing tape (used during the device singulation/dicing step).
2. The standard liquid processing during release.
3. Picking up the released device vertically either from the liquid or in air.
4. Physical transportation of the released device to be packaged.

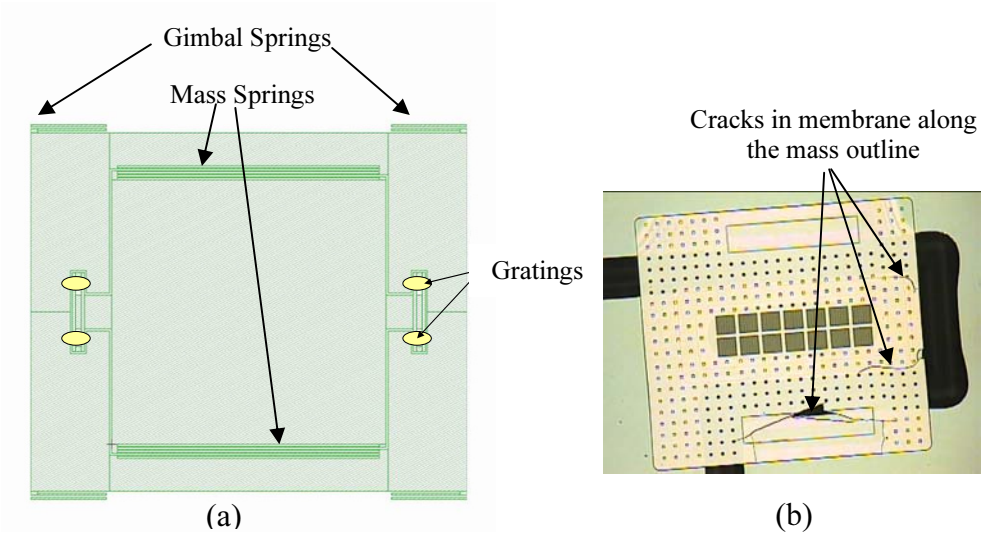

Figure 11 a) Device layout showing Mass with mechnical springs and gratings b) Released Grating membrane showing cracks along the mass outlines – possibly due to impact of mass on the membrane during handling.

3.1.1 *Failure Mechanisms:*

We analyzed both the grating membrane and the mechanical spring designs/operation to identify the failure mechanisms. We performed static analysis of spring/mass and grating membrane models to determine analytical limits in device operation.

3.1.1.1 Grating membrane failure

We modeled the thin grating membranes to identify the acceleration limits it could handle before it broke. These membranes act as springs also. We discovered that they break around 5um vertical displacement. The calculations in our model are based on maximum stress points (which are inaccurate due to bad rounding errors in ANSYS). Assuming a silicon fracture point of 0.3 GPa (Silicon Fracture point varies from 0.3 GPa – 1.7 GPa depending on literature source). So we can assume that we can safely achieve a deflection of ~ 2.5 um.

Then we performed static analysis on the mass/spring models to estimate the G loads the devices could handle (Figure 12) based on different degrees of overetch. The results are tabulated in Table 1 and shown in Figure 13.

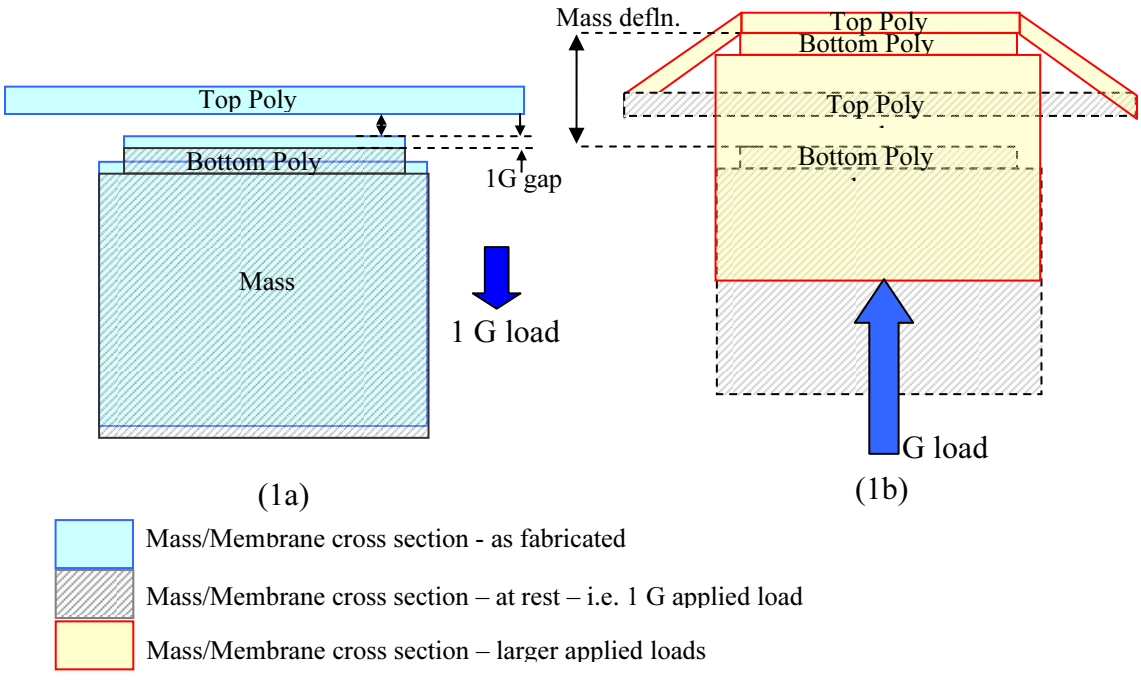

Figure 12 Cross section of membrane area showing the separation between the two poly layers that constitute the grating both a) at rest i.e. 1G applied load and b) after application of an applied G load showing bending of the membrane where the mass

Overetch	1 G load gap	Applied load	Mass deflection	Membrane Deflection
0	0.125 um	5G	0.624 um	0
0	0.125 um	10G	1.25 um	0.63 um
0	0.125 um	15G	1.87 um	1.25 um
0	0.125 um	20G	2.5 um	1.88 um
0	0.125 um	25G	3.12 um	2.5 um
3 um	0.16 um	10G	1.58 um	0.92 um
3 um	0.16 um	15G	2.37 um	1.71 um
3 um	0.16 um	20G	3.16 um	2.5 um
5 um	0.19 um	10G	1.89 um	1.2 um
5 um	0.19 um	15G	2.83 um	2.14 um
5 um	0.19 um	20G	3.77 um	3.08 um
8 um	0.26 um	5G	1.29 um	0.53 um
8 um	0.26 um	10G	2.57 um	1.81 um
8 um	0.26 um	15G	3.86 um	3.10 um

Table 1 Summary of grating membrane deflection vs. applied loads for varying degrees of spring overetch

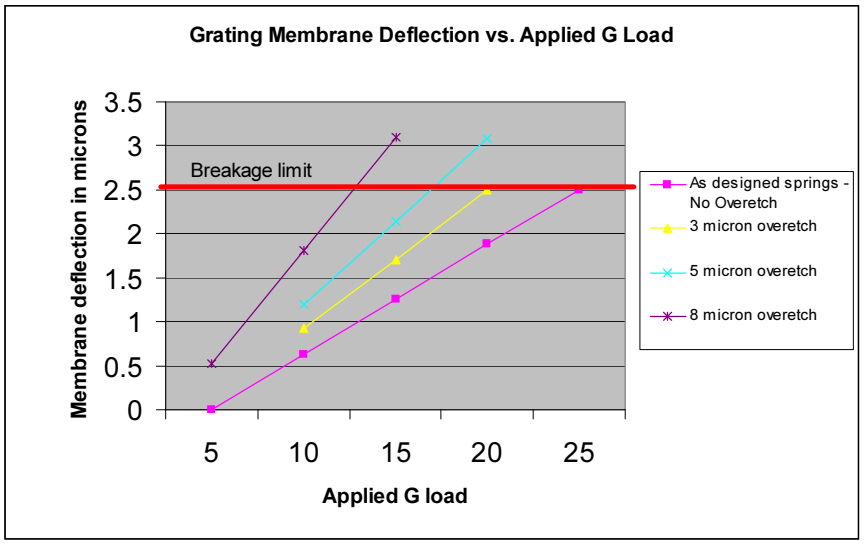

Figure 13 Grating membrane deflection vs. applied loads for varying spring overetch in the DRIE

Since our spring overetch is closer to 8um, this analysis shows us that the device can handle ~12.5G of acceleration before the membrane displacement exceeds its break point.

3.1.1.2 Mechanical Spring failure

We created a spring stress model to investigate spring failure during handling. The 2D and 3D models were used to verify stresses and to look at the significance of acceleration on mechanical springs (decoupled from the mass).

The models showed us that although the gimbal springs could handle very high g-loads in the z-direction (out-of-plane), relatively small displacements (10 microns) out-of-plane can cause them to break. Comparatively, the mass springs could handle up to 138 microns of out-of-plane displacement before breaking. Hence if the forces during the release process are significant, spring failures can occur that are completely unrelated to the acceleration. The fracture strength of silicon is highly dependent on the size of micro cracks. This could be as low as 300 MPa, while the fracture strength of bulk silicon can also be ~5-7 GPa. Hence the presence of cracks in the silicon from previous processing steps (DRIE) along with strong capillary forces could significantly weaken the springs causing them to break easily during handling.

A 2D model of the mass and gimbal with springs was used to analyze the effect of style applied accelerations on stress (Fig. 14).

- An acceleration of 0.35 G in the y-direction displaced the mass by the entire gap (30 um) and the related stress was very low (3.86 MPa) in the mass springs.
- An acceleration of 10 G in the z-direction produces a 2.56 μm displacement and a stress of 5.57 MPa in the mass springs. If we assume the device breaks at ~300 MPa, assuming linear behavior, the device would need to move about 138 μm to reach a stress of 300 MPa - corresponding to an acceleration of 539 g's.
- An acceleration of 10 G in the x-direction (nonlinear analysis) results in the mass moving 0.288 μm in X, and a stress of 1.27 MPa in the mass springs

Again, these stress levels are too low to cause breakage for normal handling conditions (~10 G accelerations). Hence we created a contact model to look at the stresses in the frame springs if they were stuck to the substrate edge. The results show substantial increase in stress, and it is feasible that the springs could break under this condition (if the forces are strong enough to cause this amount of stiction). The attached figure shows the stress distribution.

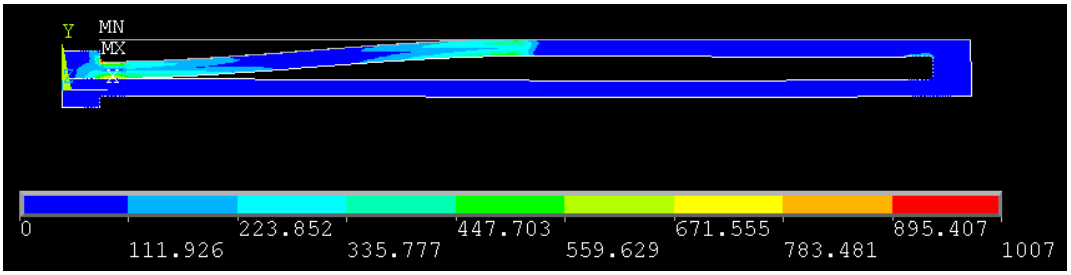

Figure 14 Ansys simulation results showing large stress levels in the spring (~1GPa) under stiction conditions (commonly observed in our pre-released fabricated samples).

3.1.2 *Observations*

Our samples were previously fabricated under the NanoG accelerometer LDRD project. These devices had been fabricated in the Sandia MDL and had undergone DRIE etch to pattern proof masses, gimbals and associated mechanical springs. The DRIE etch was a through wafer etch where the wafer thicknesses were ~ 675um.

Our starting device wafers for the Integration LDRD:

- Unreleased un-mounted device wafers
- Unreleased wafers mounted on another silicon wafer with wax

We observed a large number of samples with springs stuck to the edges prior to release. These samples had been through the final DRIE etch and had been sprayed with acetone to remove the photoresist from the surface. A large number of devices failed as they experienced varying forces during the following steps that included mounting on a silicon wafer, dicing, releasing, transporting and packaging.

3.1.3 *Dicing methodology*

Dicing is an especially harsh environment for fragile devices. Both the dicing saw and the slurry jet used to keep the wafer cool during dicing introduce a large amount of uncertainty in the forces the devices are subjected to. We observed large number of cracks and broken devices after subjecting our wafers to a relatively standard dicing process. Hence we experimented with different mounting and protection schemes to minimize damage to the device wafers both during dicing and while removing device die from the dicing tape. These included experimenting with

i) a variety of dicing tapes with different adhesion levels,
ii) using PEG (Poly-Ethylene-Glycol) to bond the device wafer to the support wafer and
iii) protection schemes for the front-side of device wafers.

We used UV cure tapes with low adhesion levels. We then mounted the device wafer on a dummy silicon wafer using PEG. The advantage of PEG is that it dissolves well in hot water and is easy to remove compared to other options that include different

waxes and photoresist. The one problem we discovered with PEG was that the resulting bond was not as good as we had hoped. There was some relative motion between the dummy wafer and the device wafer during dicing that resulted in some cracks and lowered the yield. We hand-coated the front of the device wafer with a thick layer of photoresist. Additionally we placed dicing tape on top of the photoresist for additional protection during dicing. Also we had to experiment with different baking times/conditions for the photoresist because the PEG melted at temperatures as low as 70 Celsius.

3.1.4 *Release methodology*

The release step involved the removal of the sacrificial silicon-dioxide layer to allow our devices to move freely. Since the devices were very sensitive, removal of this oxide layer implied a high degree of device vulnerability to damage post-release. We also observed the devices were very susceptible to damage in the liquid transfer/handling stage of release and in normal manual transfer steps after release.

We attempted a completely dry release to eliminate problems associated with liquid transfers. A timed HF vapor was used instead of a wet release. However, this method did not work very well. It left a residue from the release that could only be removed by immersing in liquid 49% HF – defeating the purpose of a dry release.

We proceeded to develop a careful handling plan to minimize extraneous forces applied on the device during and immediately after release. This included

i) Mounting device chip on a larger silicon chip with minimum OCON-199 wax - for support through the wet HF release.
ii) The device chip was never lifted out-of plane. It was always slid sideways from one surface to the next.
iii) Soaking in 49% HF for ~15 minutes.
iv) After release, the wax used for the silicon mount was removed by soaking in opticlear for a long time (~80 hours in some cases)
v) The device chip on the mount (without wax) was soaked in IPA and dried by placing the sandwich in a supercritical CO_2 (SCCO) chamber.
vi) The device chips were left on the silicon support mount and transported to be packaged.

For the device wafers mounted on support silicon wafers using PEG, the chip "sandwiches" were soaked in the PRS-3000 to remove the hardened Photoresist and then soaked in de-ionized (DI) water to remove the PEG. After removing the PR and the PEG, the die release process was similar to that outlined in i) - v).

Wafers that were pre-mounted with Z71 wax on a silicon wafer as part of the DRIE (BOSCH) etch were especially hard to process. We were not successful in removing all the wax, hence leaving a lot of residue on the surface and destruction of all devices on the wafer.

3.1.5 *Transportation*

We discovered that many devices did not survive careful hand transportation from the MDL release labs to the packaging labs across the tech area. We used 2" and 6" plastic single wafer holders to transport these released device chips that were sitting on silicon supports (but not attached to them). The device chips tended to slide off the support silicon and land inside the package breaking springs and gratings in the process. Hence we had to prepare packages to prevent this motion. We used 6" plastic single wafer holders and used full 6" wafers as dummy silicon supports. We proceeded to place strips of tape around the device chip to create a physical barrier on the silicon surface. This, along with careful hand transportation was adequate to prevent the devices from breaking further.

3.1.6 *Packaging Methodology*

Since our released devices were too fragile to handle, they needed to be packaged before they could be subjected to testing.

Considering the complication in redesigning our devices with built-in stops to limit motion of the proof mass, we chose to integrate such stops into the package. Since the device is a through-wafer structure, we needed to provide an open window over the mass to allow motion. Also, since we use optical sensors to measure the motion/acceleration, we needed open windows to address the sensors with external laser sources and detectors.

The goals of our packaging effort were to:

- provide a platform for die to enable easier handling to help avoid situations that would put the die under unacceptably high mechanical shock
- enable clearance for proof mass and access to optical gratings
- control gap between package and die to limit motion of the device to < 5μm to prevent breakage of the grating membrane

Our first package design, we used a sandwich approach with cross-member stop (Figure 15). The package consisted of two identical pieces of alumina – supports for both the top and bottom of die. The alumina pieces were laser cut with a high power CO_2 laser. First, the top package piece was attached while device die was still sitting on silicon support substrate. Then the die was slid off silicon substrate while holding the top package. Finally, the die was then flipped over and the bottom package piece attached to it. The distance between die and substrate was set by the epoxy bond line thickness which was hard to control to ~10-20 μm.

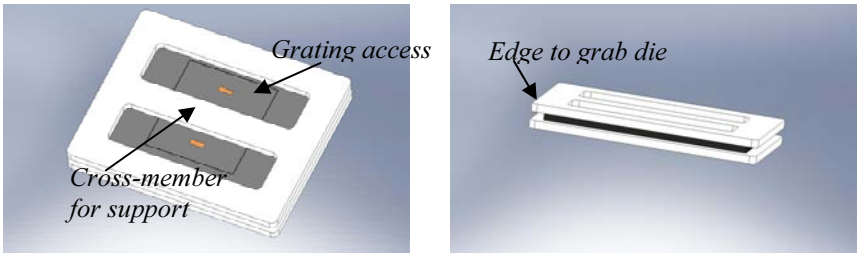

Figure 15 package design with cross-member support and access holes for optical gratings

Unfortunately, the roughness of the alumina combined with the bowing of the cross-member caused the package to "drag" on the device surface, introducing friction and impeding motion. We changed the package design to remove the cross-member and add "tabs" above the location of the device mechanical springs instead. A surface analysis (with the WYKO interferometer) of the alumina pieces showed roughness/bowing beyond the tolerances of our gap designs (~23 μm peak-to-valley in some packages) (Figure 16).

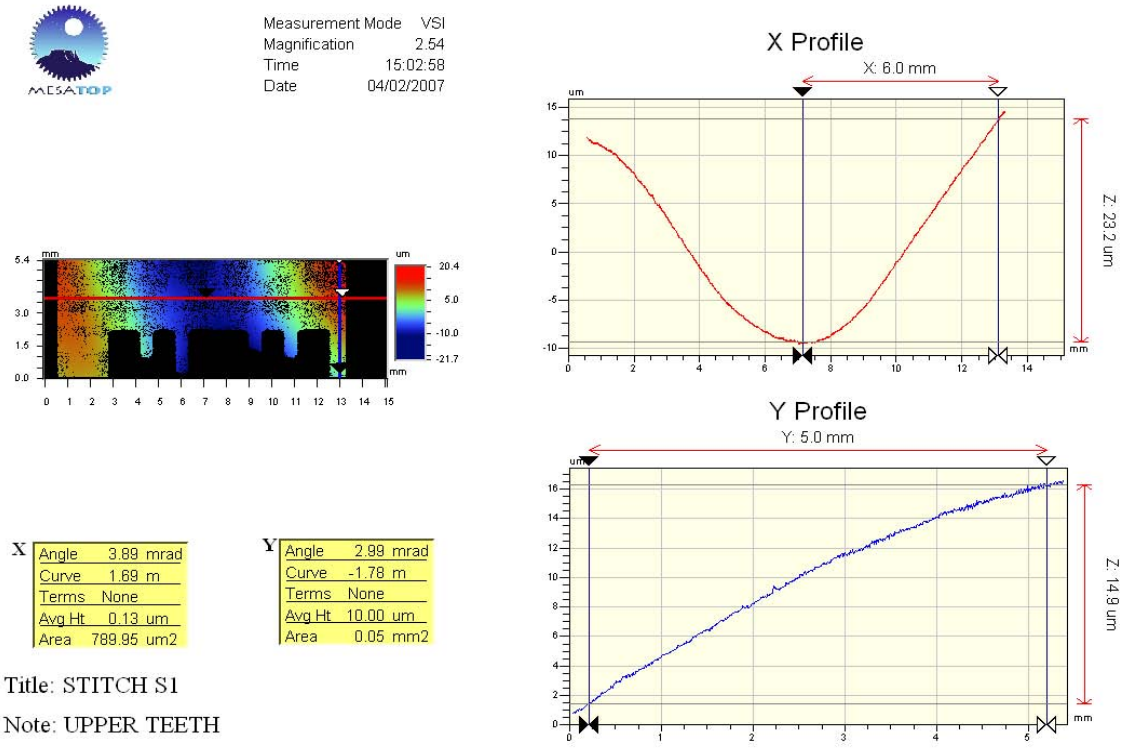

Figure 16 WYKO Analysis of alumina package showing roughness and peak-to-valley curvature of 23.3 μm on the alumina surface.

Since these curvatures in the alumina material were hard to control and were beyond the 2-5µm gap needed between the package and the device, we chose to use a flatter material – quartz. The bow in the alumina cross-member could be significant also to meet these specifications.

In our new design we chose to replace the cross-member with tabs over the device mechanical springs (Fig. 17). The quartz pieces are laser patterned (with the CO_2 laser). We also investigated building a package that could withstand the HF release. This would allow us to package the device while it was relatively less vulnerable and simplify the subsequent handling. Making an HF-resistant package involved the use of an HF resistant epoxy and HF resistant/HF-protected material. Also the quartz would be coated with a layer of silicon nitride thick enough to withstand most of the HF etch and create a 3-5 um etched gap under the device. The HF-resistant epoxy had to be applied on the edges of the package to prevent wicking under the device and increasing the bond-line. Increasing the bond-line would increase the gap, increasing the shock seen by the device. Unfortunately, we were unable to apply the edge-based epoxy without increasing the bond-line (with epoxy wicking under the device). However, it is conceivable that we could have improved on these results given the right resources.

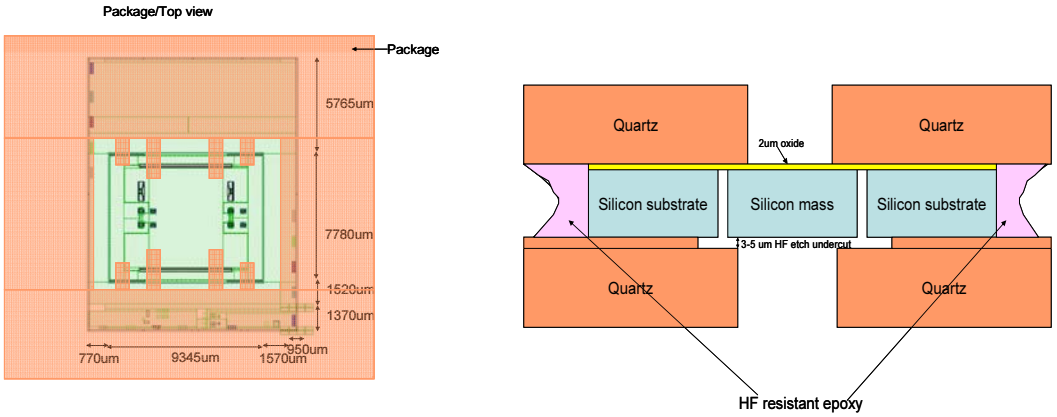

Figure 17 a) New package design in quartz showing 'tabs' over mechanical springs b) Cross-secion of proposed package showing edge-based epoxy application and 3-5 um engineered undercut of the quartz package under the device.

In the absence of the right resources to pursue this solution further, we chose to attach the quartz package to the device after release since quartz etches very fast in Hydrofluoric acid. The packaging steps we followed are outlined in figure 18. Care was taken to minimize the bond line as best possible. A photograph of a packaged device is shown in Figure 19.

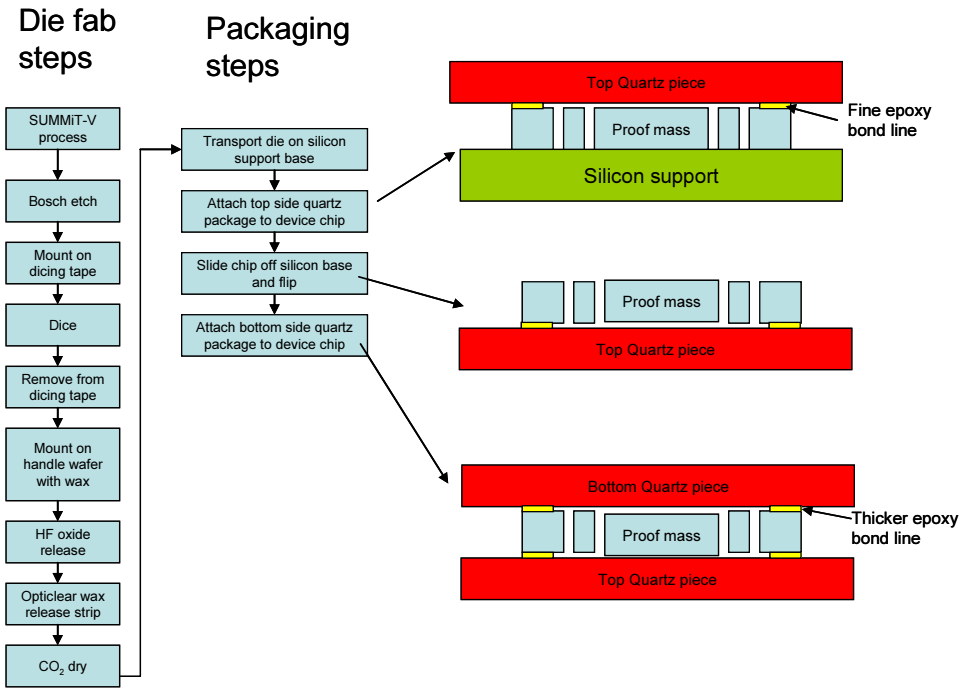

Figure 18 Process flow showing packaging steps.

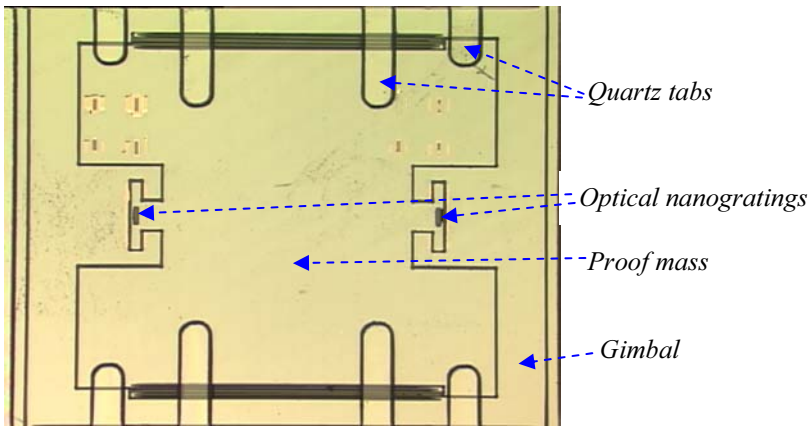

Figure 19 Photo of packaged die showing mechanical quartz tabs over the mechanical springs to limit the out-of-plane motion of the proof mass and

3.1.7 *Testing:*

Finally, we tested our packaged accelerometer with a large mass design (33.6 mg). We used a Laser Doppler Vibrometer (LDV) and shaker table to perform dynamic mechanical tests on these devices. We measured resonant frequencies ~36 Hz (Figure 20).

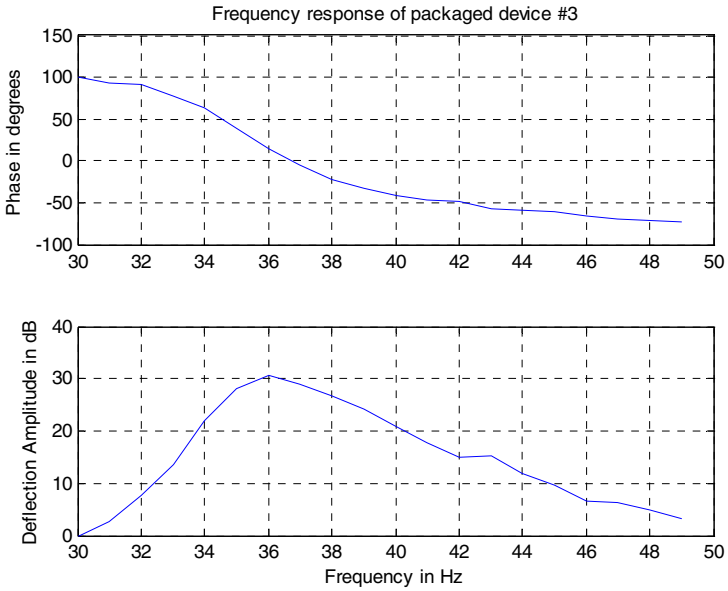

Figure 20 Phase/Amplitude frequency response characteristics (in air) for packaged nanograting accelerometer 33.6 mg Mass (device 3)

To the best of our knowledge, these are the lowest resonances for MEMS accelerometers measured to date.

We proceeded to build an optical setup to measure the optical output from our integrated nanograting sensor (Figure 21). We used an 850nm laser diode, several beam splitters and custom reference detection circuitry. We used a high precision 3-axis piezo-controlled flexure stage (Nanomax™ from Thorlabs Inc. with 5nm resolution) to provide the extremely small displacements/accelerations needed. The intensity of the optical beam reflected from the integrated nanograting sensor was measured with the photodetector circuitry and correlated with the applied acceleration.

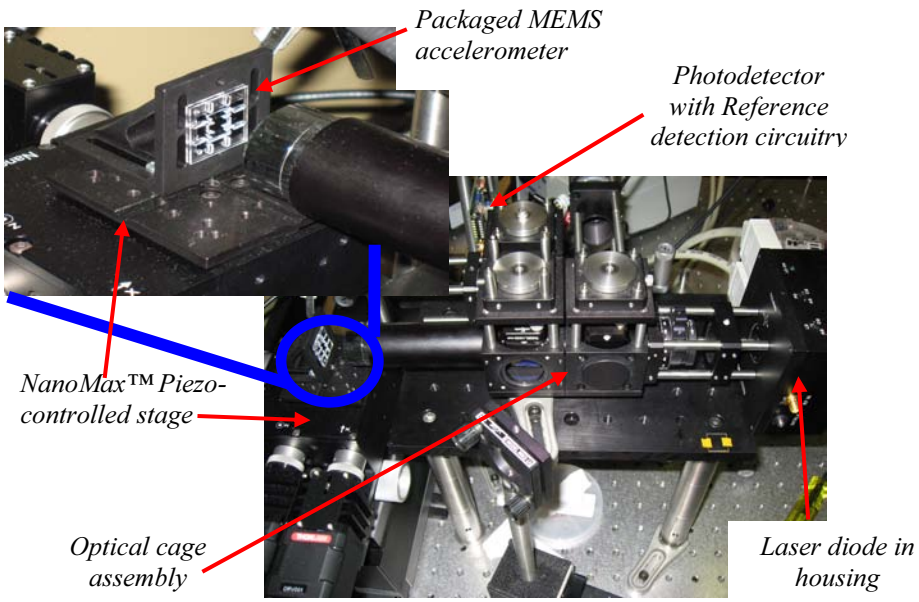

Figure 21 Experimental setup for optical testing of nanograting accelerometers showing packaged device, optical setup, 5nm resolution piezo-actuation stage and photodetector with reference detection electronics.

We directly measured output signals ~3.80 mV for applied accelerations as small as 6.45μG. This corresponds to a sensitivity of ~ 589V/G. The noise floor was measured at ~ 10μV/√Hz (Figure 22). This corresponds to a noise floor of ~ 17nG/√Hz. The theoretical thermal noise floor was calculated, based on the equation below, to be 8nG/√Hz.

$$a_{noise,rms} = \sqrt{\frac{4k_b T\omega_0}{mQ}}$$

To the best of our knowledge, these are the most sensitive MEMS accelerometers built to date and are 40dB more sensitive than the best reported in-plane MEMS accelerometers [2-3].

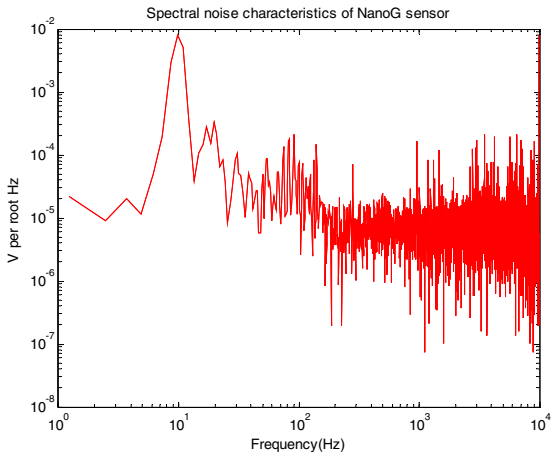

Figure 22 Noise spectra of the Nano-G accelerometer. This corresponds to a sensitivity of ~ 589V/G. The noise floor was measured at ~ 10μV/√Hz. This corresponds to a noise floor of ~

3.1.8 *Yield improvement/recommendations:*

Dicing:

- We noticed that PEG was the easiest to remove compared to all other mounting options for the device wafer on a silicon substrate.
- We also hand-coated the top side with photoresist and there was no need to attach dicing tape to the top surface of the wafer for extra protection.

Packaging:

- Consider packaging right after dicing and before the HF release process.
- Use Quartz packaging pieces coated with silicon nitride. Engineer the nitride thickness to withstand HF release process. This provides the package transparency, flatness along with the necessary ruggedness.
- Engineering the nitride thickness will allow control of the quartz etch to create a finer gap (~2-5 um) between the device and the package during the standard release step.
- Other option is to use Sapphire pieces instead of quartz since they do not etch well in HF but have both the flatness and transparency properties of Quartz.

Design:

- A larger space between the springs and the frame/mass would require there to be a larger force to make the springs stick to the edges, and therefore may be a way of reducing this problem.
- Adding a layer of polysilicon above the gratings as a built-in stop for the device would limit the effect of large transient accelerations/forces.
- A more complex Bosch etch mask to leave some relatively thin “tabs” holding the mass and gimbals in place and attached to the substrate through release and packaging would be useful. The “tabs” can be removed later with a laser ablation process or the like.

3.2 Fraunhofer diffraction accelerometers

Part of this LDRD supported the work to incorporate a proof mass into the microphone process flow. This created an accelerometer designed on far-field diffraction effects. The operation of the diffraction grating can be found in the SAND report for the LDRD (93518) [Hall]. A summary of the diffraction principles follows. When light illuminates a series of lines and spaces, a diffraction pattern is formed at a distance large compared with the wavelength as a result of Huygen's principle. A representative diffraction pattern from a grating can be seen in figure 23.

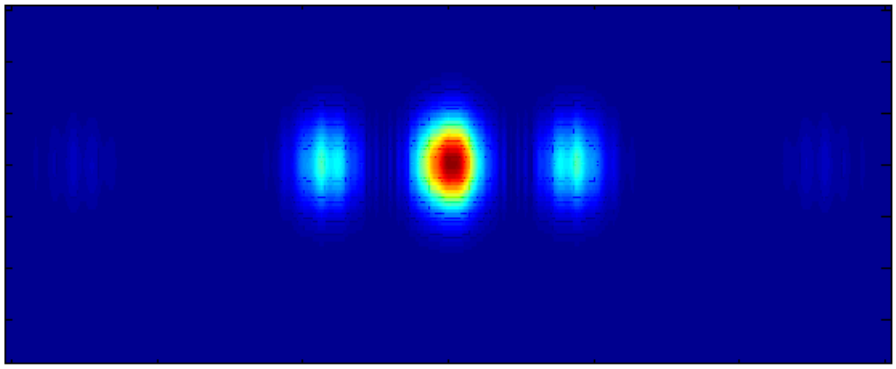

Figure 23 Diffraction pattern resulting from a 2 μm line and spacing grating at a 1 mm viewing distance

The bright center spot represents the 0^{th} order diffraction spot while the area on the left and right represent the 1 and -1 order. The signal transduction from the light is discussed below. Following is a summary of the design changes required to change a microphone into an accelerometer, and the new design that evolved from the original. The primary goal of the new design was to reduce processing steps and improve optical access to the diffraction gratings.

3.2.1 *Back-side access membrane accelerometer*

The microphones were designed and fabricated using the SwIFT™ process. This is a multilayer, planarized stack of silicon nitride, silicon dioxide and polysilicon. The diffraction gratings were fabricated in a silicon nitride layer suspended approximately 2 μm under another silicon nitride layer. The top nitride layer is solid. The back of the wafer is etched away to leave the two nitride layers suspended over an air gap. The diffraction grating is illuminated from the back side of the device. The top nitride layer serves as a reflective layer, sending the diffracted light back out through the etch hole. The light is then captured in photodiodes and the electrical signals used to analyze the motion of the membrane. When the membrane is displaced (by pressure waves or other causes), the boundary conditions for constructive and destructive interference in the diffraction grating change. These changes cause intensity variations in the diffraction orders, which modulate the output current from the photodiodes. The output signals are recorded and analyzed to determine the motion of the membrane.

In order to convert this structure into an accelerometer, a new design was fabricated. This design left part of the wafer attached to the suspended membrane. When this mass was subjected to an acceleration, the membrane would deflect. This modulated the intensities of the diffraction orders, which would change the output currents from the photodiodes. A schematic cross section of the device can be seen in figure 24.

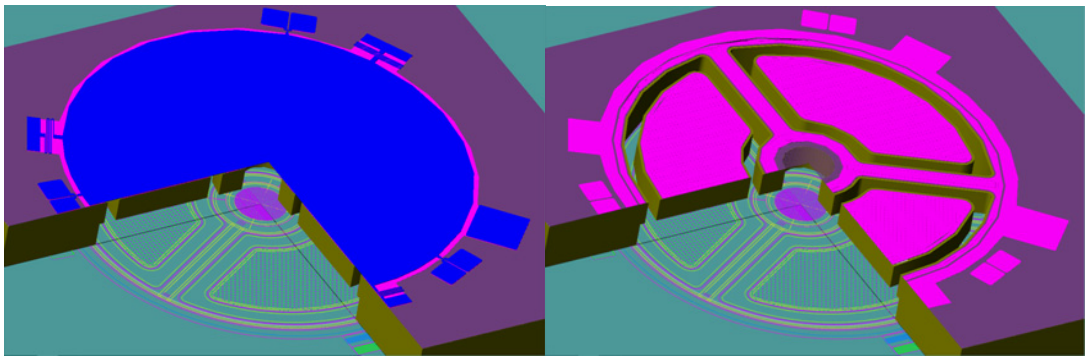

Figure 24 Schematic of the accelerometer with membrane on top and with the membrane removed.

Fabricated devices that were released can be seen in figure 25. The microphone had the entire membrane suspended by the edges. This created a rigid connection to the wafer. The sensitivity of accelerometer is proportional to the resonant frequency. The resonant frequency for a membrane is larger than that for the same size structure with only several anchors along its perimeter. Therefore, to enhance the sensitivity, the membrane was anchored to the substrate via springs. These can be seen in Fig 25.

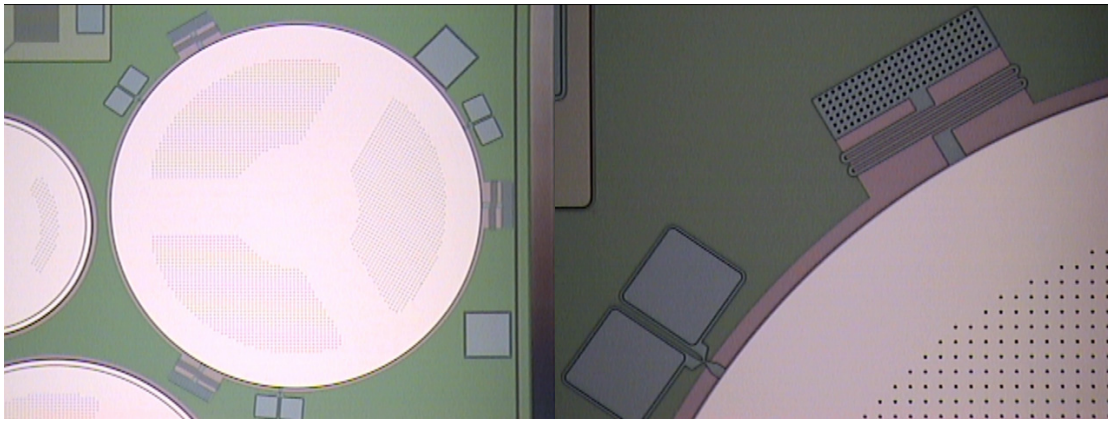

Figure 25 Optical picture of the accelerometer. The enhanced photograph shows the spring attachments to the anchor the membrane to the substrate. These springs lowered the resonant frequency of the structure to enhance its acceleration sensitivity.

These devices were illuminated from the back side. The membrane caused the diffraction pattern to return through the backside hole. Problems arose with this design because the divergence of the light source used to illuminate the gratings. A gas laser has a divergence of approximately 1 mrad. The divergence of the VCSELs used in the

measurement is approximately 175 mrad. The extra divergence coupled with the path length the light traveled to and from the diffraction grating caused the diffraction orders to overlap on the photodiodes. The overlap reduced the change in current from the photodiodes when the membrane deflected. This resulted in a lower sensitivity of the accelerometer.

3.2.2 *Front-side access membrane accelerometer*

The second design of the membrane diffraction accelerometer had the grating suspended over the membrane. This allowed optical access from the front of the device. By illuminating the device from the top, the mass on the back of the membrane encompassed the entire device. A small annular ring was etched through the wafer to release the large cylindrical proof mass hanging under the diffraction grating. A schematic of the device can be seen in figure 26.

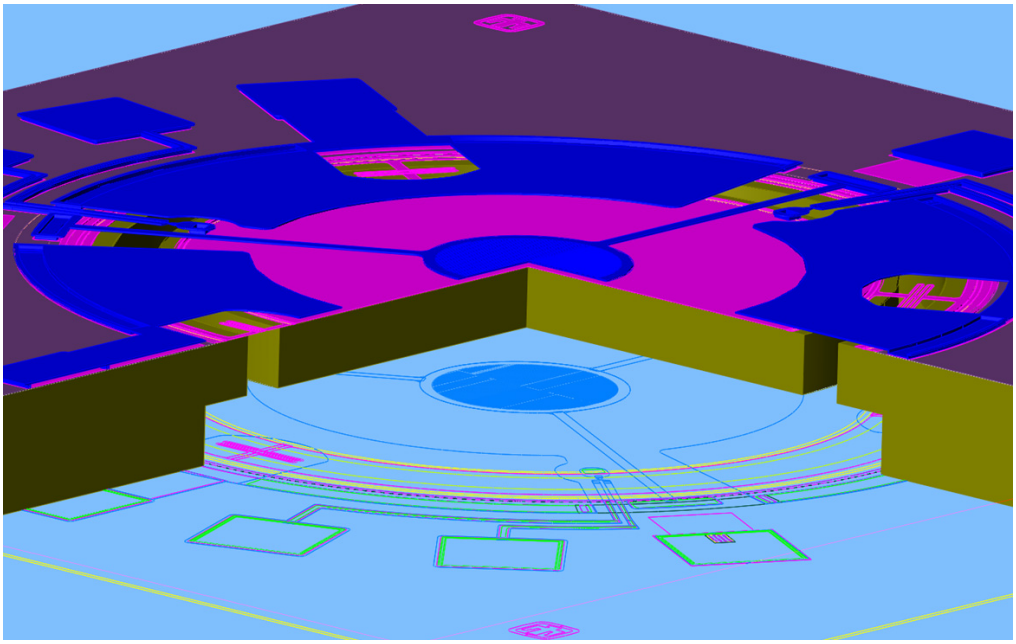

Figure 26 Schematic of the accelerometer with front side access. A large proof mass is suspended by three springs (pink). The diffraction grating is suspended over the device (blue).

In order to model the sensitivity of the accelerometer, finite element simulations were performed on the springs and mass. The suspended mass would be perfectly rigid, so it was reduced to a point mass at its center of mass. The springs were modeled using beam elements due to their ratio of length and width to thickness. The simulation model can be seen in figure 27.

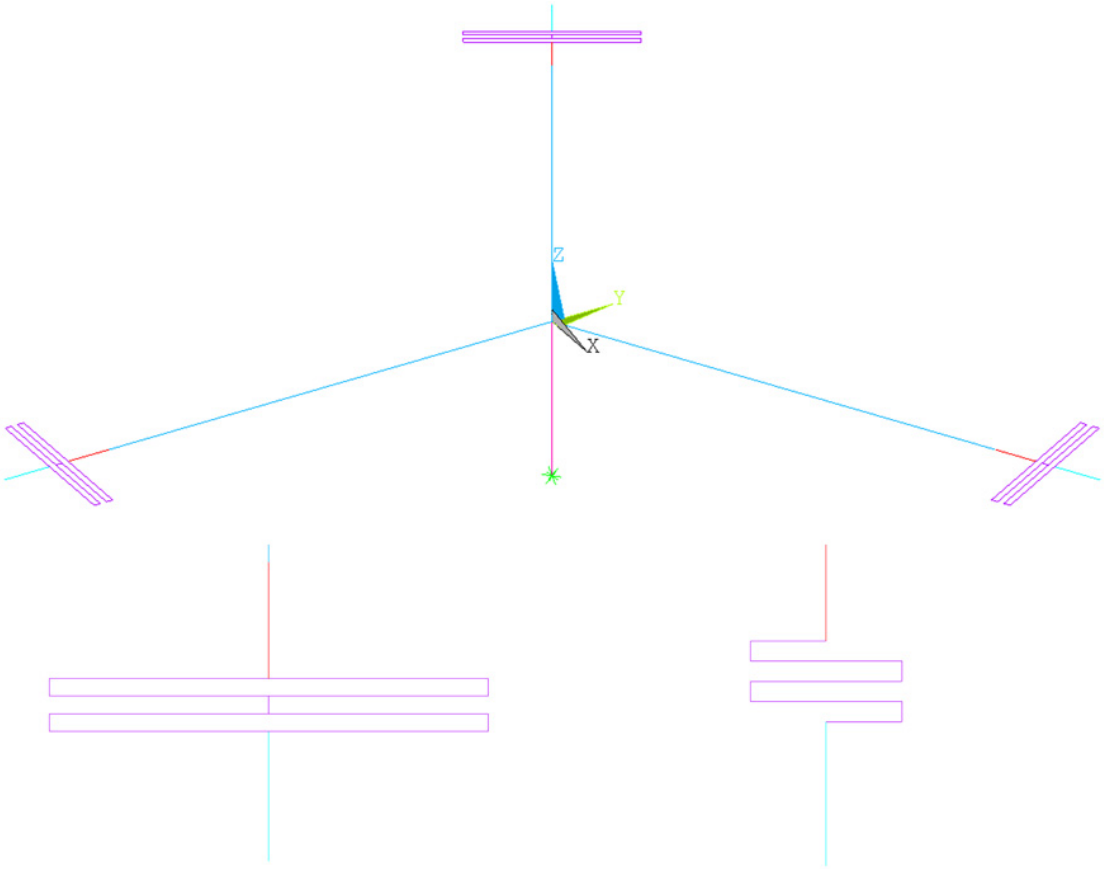

Figure 27 ANSYS simulation showing the mass centered at the middle of the cylinder. It is attached rigidly to the springs. The springs were modeled with two designs (box and meander).

Two polysilicon thicknesses of the springs were simulated for the design, 0.6 and 1.3 μm. The length of the spring from center to edge was varied from 10 to 100 μm for the thinner poly and from 30 to 100 μm for the thicker poly using the meander spring design. For the box spring design, the lengths were varied from 10 to 100 μm for the thinner poly and 70 to 160 μm for the thicker poly. The displacement of the membrane as a function of spring dimensions was simulated with a static load of 1 g on the mass. The results can be seen in Table 2.

Table 2 Table showing the displacement of the different spring designs under a 1 g load.

Box Spring				Meander Spring			
0.6 μm thick		1.3 μm thick		0.6 μm thick		1.3 μm thick	
Length	1g displacement	Length	1 g displacement	Length	1 g displacement	Length	1 g displacement
10	12.8	70	3.3	10	15.7		
20	13.6	80	4.2	20	24.6		
30	15.0	90	5.4	30	44.1	30	4.5
40	17.4	100	6.8	40	78.9	40	8.0
50	21.0	110	8.5	50	133.6	50	13.5
60	26.2	120	10.5	60	212.9	60	21.4
70	33.2	130	12.9	70	321.6	70	32.2
80	42.3	140	15.7	80	464.2	80	46.4
90	53.9	150	18.9	90	645.5	90	64.3
100	68.1	160	22.5	100	870.1	100	86.6

Additionally, a modal analysis was performed to determine the natural frequencies of vibration for both spring designs and all their respective lengths (Fig. 28).

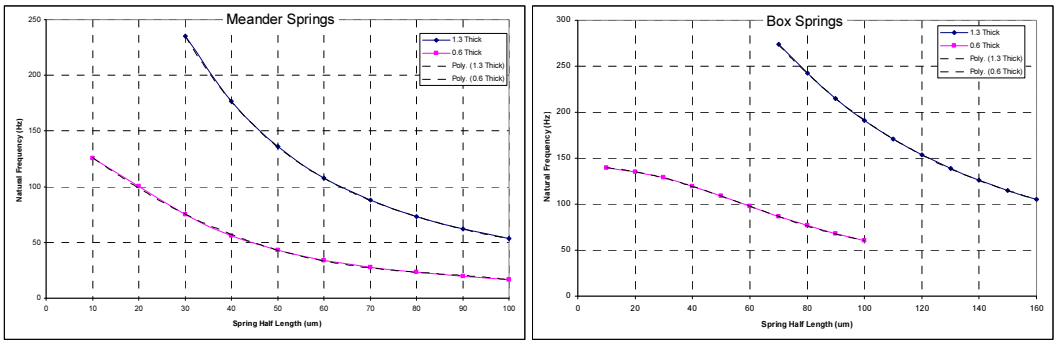

Figure 28 Graph of the resonant frequency of the structures versus spring length and thickness.

The desired Z plunge mode was the lowest frequency mode for all spring designs. A rocking motion of the top part of mass about one of the axis of the springs was the second lowest mode at approximately 20% higher frequency. The remaining modes were all at least a factor of 10 higher in frequency than these two. The second lowest mode does not produce significant displacement of the membrane below the diffraction grating. It would be excited by off-axis accelerations (not z-axis). However, these accelerations would not appear as outputs from the device because they would not couple into the desired mode because they would only be superimposed on these vibrations. Polysilicon devices fabricated using the SUMMiT process have not shown any non-linear materials behavior. Assuming small amplitudes of excitation, none of the modes would combine with other modes to produce non-linear combinations of motions.

3.2.3 *Packaging*

During the design process, several packaging schemes were contrived. The packaging schemes were designed to illuminate the gratings with light from a VCSEL, collect the light from the diffraction patterns in photodiodes, and convert it into current for signal processing uses.

Efforts were made to study devices wherein the laser diode itself became a more active piece in the sensing mechanism. Coupling the reflected light from a movable device back into the laser cavity can produce very strong nonlinear effects that are critically dependent upon the deformation in the mechanical structure. There has been some previous research performed elsewhere on interferometer devices that employ feedback (see references), and this work showed the expected behavior of a very strong dependence on relative phase of the emitted light and light that is fed back into the front laser facet. The challenge of utilizing the feedback approach is that there is considerable nonlinearity and the potential for chaotic behavior that can not be easily controlled. This makes it a high risk and high reward endeavor. Unfortunately, the knowledge gained by these studies was not recorded before the PI left to form a company (presumably based on these principles). All efforts following this event focus on eliminating the feedback into the VCSEL.

The original design of the package was to accommodate the back-illuminated accelerometer design. This design was to mount a VCSEL and photodiodes onto a low temperature co-fired ceramic (LTCC) carrier and bring the electrical leads out to the edge of the chip by electrical vias. A picture showing the mounting of a VCSEL and 3 photodiodes (PDs) can be seen in figure 29 and a larger view of the chip in the well can be seen in figure 30.

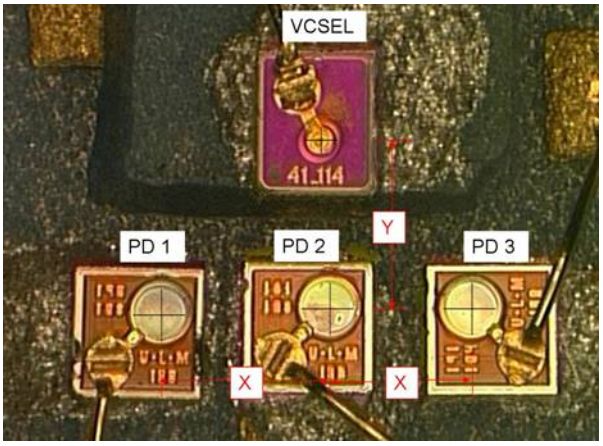

Figure 29 Optical picture of a VCSEL (top) and 3 photodiodes mounted and wire bonded to an LTCC carrier.

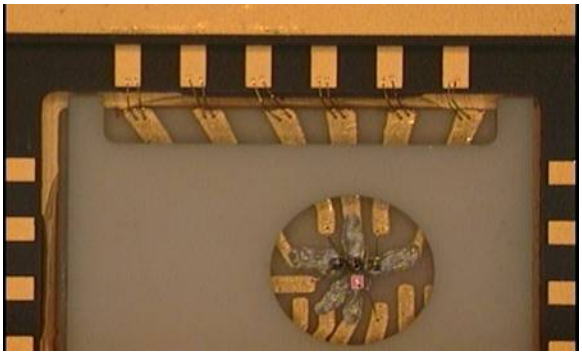

Figure 30 Optical picture of the VCSEL and photodiodes attached to the bottom well of a 24 pin DIP and wire bonded to the pins of the package.

A standoff was mounted to prevent the MEMS component from contacting the VCSEL and PDs and to provide the correct geometry to collect the light from return light from the diffraction pattern. A schematic of the orientation of the MEMS component and the optoelectronic components can be seen in figure 31.

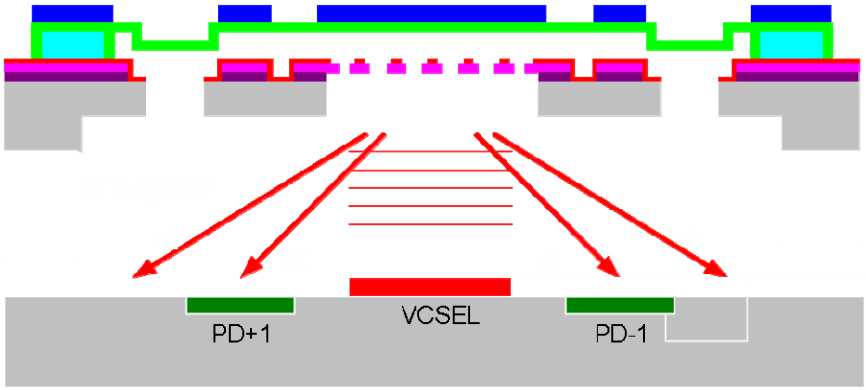

Figure 31 Schematic of the packaging design. The VCSEL would illuminate the grating from the bottom and collect the diffracted light onto photodiodes.

This design was implemented before Dustin left. It had feedback issues of the light back into the VCSEL. In order to prevent the non-linearities, two options were attempted: using a lens with offset VCSEL and PDs and tilting the VCSEL to reflect onto the PDs.

The first attempt involved offsetting the VCSEL and PDs into two rows. A lens was placed in front of the VCSEL and PDs, and directing the light from the VCSEL up to the grating and back down to the PDs. A schematic can be seen in figure 32.

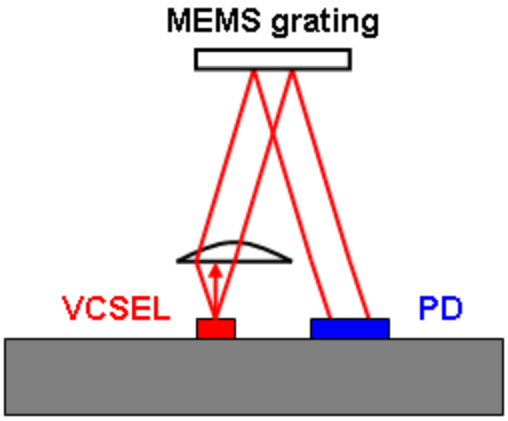

Figure 32 Schematic illustration of the use of an off-axis micro-lens to diverge the beam to an offset VCSEL.

This packaging scheme was used for several backside-access diffraction-based accelerometers. The alignment of the lens was too difficult to ensure reproducibility. Small angular and vertical offsets caused the diffraction patterns to focus off of the photodiodes. This effort was terminated due to the alignment issues.

The second packaging scheme was to tilt the incoming light with respect to the diffraction grating. This was accomplished by two methods. The first involved shimming the edge of the MEMS chip (Fig 33a), while the second involved tilting the VCSEL at an approximate angle of 15° (Fig 33b).

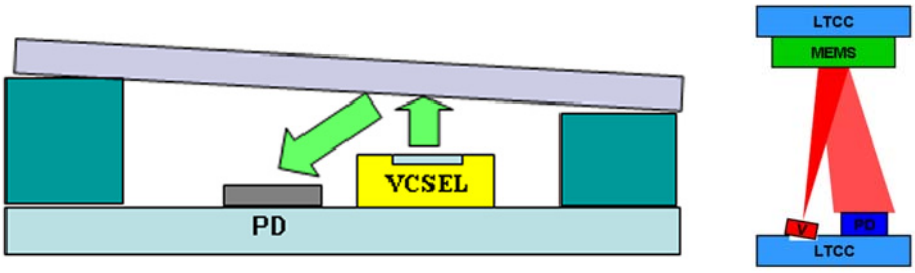

Figure 33 Schematic of the packaging scheme showing the light from the VCSEL incident at an angle with respect to the normal direction of the MEMS grating. a) In this attempt, the MEMS component is shimmed on one side to create the angle. b) In the second attempt, the VCSEL is tilted during mounting to cause the incident light to arrive at an angle.

Both of these attempts showed significant improvements in accuracy of placement and ease of alignment with the gratings. Tilting the VCSEL with respect to the normal vector of the grating was the path chosen for the final assembly.

The final assembly consists of mounting the MEMS component to a LTCC carrier with electrical leads using epoxy to secure the die in place. The electrical leads on the

LTCC connect the MEMS component to the correct pins in the DIP. Spacers of thickness slightly larger than the VCSEL and PDs are then glued to the edge of the LTCC to stand off the top LTCC. The top LTCC has the VCSEL and PDs attached to it. The VCSEL is mounted to an angled mount to prevent light feedback into the VCSEL (Fig. 34). An overhead picture of the packaged device can be seen in figure 35.

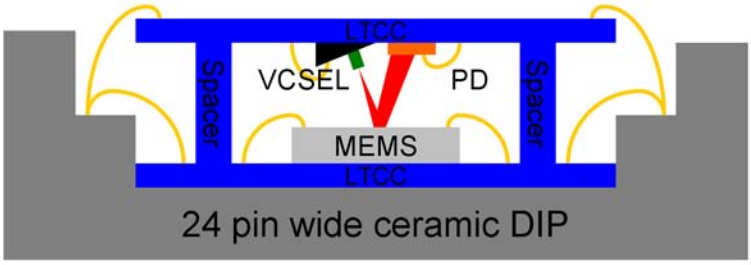

Figure 34 Schematic of the final packaging assembly. The MEMS part is attached to the bottom of a 24 pin ceramic DIP. The light source and photodiode are attached to a top LTCC carrier. After active alignment, the top LTCC is attached with epoxy to the spacer.

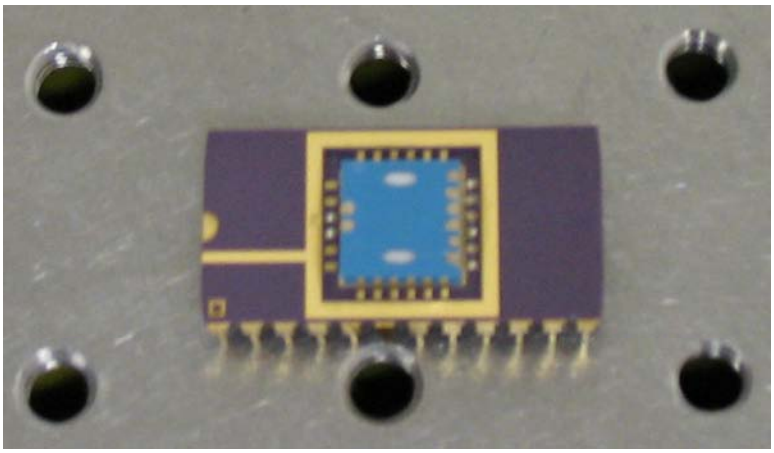

Figure 35 Picture of the MEMS component packaged in a 24 pin DIP. The DIP is sitting on an optical table with 1" on center holes.

4 CIRCUIT READOUT

During an acceleration event, the mass of the accelerometer responds to the force by moving toward or away from the grating. This causes a change in the intensity of the diffracted light, modulating the current in the PDs. In order to measure the motion of the accelerometer, the current from the PDs is sent into a circuit. The circuit has been summarized in the nano-photonics LDRD final report. A brief summary and diagram will be presented here.

A simple circuit that compares the two currents and outputs a response proportional to the difference would suffice for high frequency measurements. The frequency range of interest for the above-mentioned applications is near or below 1 Hz.

At these frequencies, there is noise in the system generated by the VCSEL, PD and device itself due to Brownian motion. A summary of these noise sources and their effects on the measurements is described below.

The layout and components of the circuit designed to cancel the noise can be seen in Fig. 36.

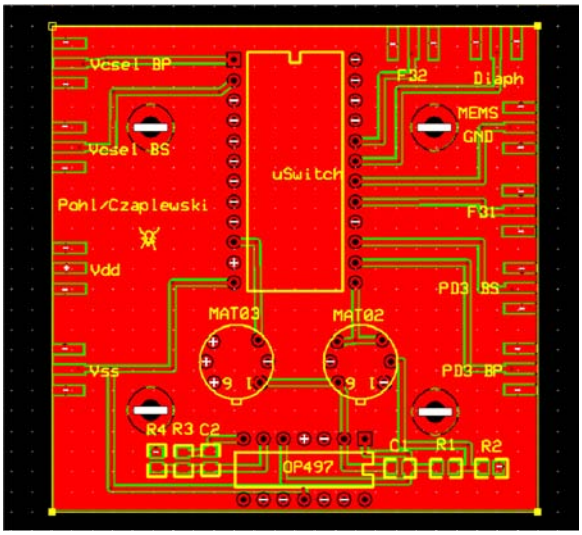

Figure 36 Layout and components of the circuit used to cancel low frequency noise in the measurements

Since our interferometric accelerometer uses an optical diffraction sensing technique, noise sources that affect the performance of our sensor include laser relative intensity noise (RIN), photodetector shot noise, electronics amplifier noise and thermal/brownian noise.

Laser relative intensity noise (RIN) is defined as the ratio of mean-square optical intensity noise to the square of the average optical power:

$$RIN = \frac{<\Delta P^2>}{P^2} \quad dB/Hz$$

where: $<\Delta P^2>$ is the mean-square optical intensity fluctuation (in a 1-Hz bandwidth) at a specified frequency, and P is the average optical power.

Shot noise is produced by the quantum nature of photons arriving at the detector, and related detection statistics. The noise produced is related directly to the amount of light incident on the photodetector. The mean-squared noise current, $<i_n^2>$ from the photodetector is:

$$< i_n^2 > = \quad 2qI_{dc}B \quad = \quad 2qI_{dc} \quad (A^2/Hz)$$

where: q is the electron charge (1.60 x 10^{-19} coulomb);
I_{dc} is the current out of the diode due to the average optical power input; and B is the electrical noise bandwidth of the measurement (typically normalized to 1 Hz).

The Operational Amplifier (OP497 BJT) used in the detection circuitry also contributes noise and can degrade the displacement/acceleration sensitivity of the device. The amplifier noise can be well below the shot noise limit through thoughtful choice of a low current noise amplifier. This noise inherent in the electrical circuitry is typically specified in the manufacturer's data sheet.

The thermal/brownian noise equivalent acceleration experienced by the proof mass can be calculated from the equation:

$$a_{noise,rms} = \sqrt{\frac{4k_b T\omega_0}{MQ}}$$

where k_b is Boltzmann's constant (1.38E-23 J/K), T is the absolute temperature in Kelvin, ω_0 is the resonant frequency of the proof mass in radians/s, and M is the mass in kg.

We performed a detailed noise analysis to determine the limits of detection for our far-field interferometric accelerometer. We assumed the following parameters for our calculations:
Incident optical power on detector (P) = 1.13 mW
Photodetector efficiency = 45 %
Reference Current, I_{ref} = 254 μA
Signal current, I_{sig} = 127 μA
Sensor response ( )= 0.5%/nm or 0.635 μA/nm
Proof Mass (M)= 5E-7 kg
Spring constant (k) = 1.5 N/m
Laser Noise cancellation = 50 dB

For these parameters, anticipated displacement response (d) of the device:

$$d = \frac{M}{k * 9.8} = 3.3e-8 \quad (m/g)$$

where 1g = 9.8m/s^2

Also, resonant frequency, $f_{res,}$ can be calculated from:

$$f_{res} = \sqrt{\frac{k}{m}} = 1.732 \quad (kHz)$$

And typical measured Q = 100

The following table (Table 3) shows noise equivalent acceleration calculations at 10Hz for our device without any special noise cancellation circuitry:

	Noise at Isig (A^2/Hz)	Noise at Isig (A/√Hz)	Displacement (m/√Hz)	acceleration (g/√Hz)
Laser RIN	6.31E-13	7.94E-07	1.25E-09	3.75E-02
PD Shot Noise	4.00E-23	6.32E-12	9.96E-15	2.99E-07
OP497 BJT Amp. Current Noise	1.6E-25	4E-13	6.3E-16	1.89E-08
Brownian Noise	-	-	-	7.58E-07
Total Noise	-	-	-	***0.037529***

Table 3 Noise equivalent displacement/acceleration calculations at 10Hz without external noise cancellation circuitry

We have demonstrated 60dB noise cancellation with our Hobbs Circuit [5]. While this reference detection circuit cancels laser RIN, the noise contributions due to shot noise and amplifier noise increase. With this noise cancellation circuitry, the performance achievable with our device is shown in table 4 below:

	Noise at Isig (A^2/Hz)	Noise at Isig (A/√Hz)	Displacement (m/√Hz)	acceleration (g/√Hz)
Laser RIN	6.31E-19	7.94E-10	1.25E-12	3.75E-05
PD shot Noise	1.6E-22	1.3E-11	2E-14	6E-07
OP497 BJT Amp. Current Noise	1.6E-25	4E-13	6.3E-16	1.9E-08
Brownian Noise	-	-	-	7.6E-07
Total Noise	-	-	-	***3.8E-05***

Table 4 Noise equivalent displacement/acceleration calculations at 10Hz with Hobbs noise cancellation circuitry

Reference:

[5] R. H. Olsson III, B. E. N. Keeler, and D. W. Carr, "Circuit Techniques for Reducing Low Frequency Noise in Optical MEMS Position and Inertial Sensors," *IEEE International Circuits and Systems Conf.,* pp. 2391-2394, May 2007.

5 CONCLUSION

This work had the goal of realizing the integration of MEMS accelerometers with opto-electronic components into a complete packaged device. In order to achieve this goal, two separate MEMS technologies were investigated: a nano-photonics grating accelerometer and a diffraction-based accelerometer. Both of these technologies are a result of other LDRD programs.

This work helped the nano-photonics grating LDRD (67023) realize an accelerometer design by integrating a proof mass with the grating structure. Following the fabrication of this device, extensive efforts were made to release the structure without damaging the grating. The main lesson learned was to rigidly hold the device during release and drying. Ultimately, a die was released and measured without integration. We directly measured output signals of approximately 3.80 mV for applied accelerations as small as 6.45μG. This corresponds to a sensitivity of ~ 589V/G. The noise floor was measured at ~ 10μV/√Hz. This corresponds to a noise floor of approximately 17nG/√Hz. The theoretical thermal noise floor was calculated to be 8nG/√Hz. The program ended before we were able to package this device with a VCSEL and PDs to realize a fully integrated sensor.

The second MEMS technology came from the ultrasensitive directional microphone arrays for military operations in urban terrain and future combat systems LDRD (93518). This application utilized a diffraction-based sensing technique with different optical component placement and a different detection scheme from the nano-g accelerometer. The Integrated NEMS LDRD supported the microphone array LDRD by providing custom designs, VCSELs, and measurement techniques to accelerometers that were fabricated from the same operational principles as the microphones, but contain proof masses for acceleration transduction. These devices were packaged at the end of the work.

6 FUTURE WORK

The work done in this LDRD leads into several areas of interest. The nano-photonic gratings are being investigated for optical filter applications. The packaged accelerometers are being investigated for several applications that can be addressed by the PI or PM but cannot be discussed in this open forum.

7 REFERENCES

[1] SAND 2006-6534, U. Krishnamoorthy, D.W. Carr, G.R. Bogart, B.E.N. Keeler, R.H. Olsson III, A.A. Talin, L.L. Hunter, M.C. Warren, "NanoG accelerometer using nanophotonic motion detection system", printed 08/2007.

[2] B. V. Amini and F. Ayazi, "Micro-gravity capacitive silicon-on-insulator accelerometers," *J. of Micromech. and Microeng.,* vol. 15, pp. 2113-2120, 2005.

[3] J. Chae, H. Kulah, and K. Najafi, "A monolithic three-axis micro-g micromachined silicon capacitive accelerometer", *J. Microelectromech. Syst.,* vol. 14, no. 2, pp. 235-242, 2005.

[4] N. A. Hall, M. Okandan, R. Littrell, D. Serkland, G. Keeler, K. Peterson, B. Bicen, C. Garcia, and F. L. Degertekin, "Micromachined accelerometers with optical interferometric read-out and integrated electrostatic actuation", (submitted to Journal of Microelectromechanical Systems).

8 PUBLICATIONS

8.1 Journal

1. U. Krishnamoorthy, D.W. Carr, G.R. Bogart, M.S.Baker, R.H. Olsson III "In-Plane Nano-G Accelerometer based on an Optical Resonant Detection System", Technical Digest, Transducers 2007 conference, June 2007, Lyon, France.

2. U. Krishnamoorthy, D.W. Carr, G.R. Bogart, M.S.Baker, P. J. Clews, T. P. Swiler, R.H. Olsson III, " In-plane MEMS-Based Nano-G accelerometer with Sub-Wavelength Optical Resonant Sensor", invited submission to Sensors and Actuators A: Physical Journal. (July 2007). [Peer Reviewed]

3. R. H. Olsson, B. E. N. Keeler, D. A. Czaplewski, D. W. Carr, "Circuit techniques for reducing low frequency noise in optical MEMS position and inertial sensors", Technical digest, 2007 IEEE International Symposium on Circuits and Systems, May 27-30, 2007, New Orleans, LA, USA.

4. N. A. Hall, M. Okandan, R. Littrell, D. Serkland, G. Keeler, K. Peterson, "Micromachined accelerometers with optical interferometric read-out and integrated electrostatic actuation", (submitted to JMEMS). [Peer Reviewed]

8.2 Conferences:

1. U. Krishnamoorthy, D.W. Carr, G.R. Bogart, M.S.Baker, R.H. Olsson III "In-Plane Nano-G Accelerometer based on an Optical Resonant Detection System", Transducers 2007 conference, June 2007, Lyon, France.

2. T.P. Swiler, U. Krishnamoorthy, P.J. Clews, M.S. Baker, D. Tanner, "The Challenges of Designing and Processing Extreme Low-G MEMS Accelerometers", Submitted to SPIE MOEMS/MEMS, Jan 2008. (Aug 2007)

3. Invited abstract submission in progress for IEEE NEMS 2008 conference.

4. R. H. Olsson, B. E. N. Keeler, D. A. Czaplewski, D. W. Carr, "Circuit techniques for reducing low frequency noise in optical MEMS position and inertial sensors", 2007 IEEE International Symposium on Circuits and Systems, May 27-30, 2007, New Orleans, LA, USA.

9 INTELLECTUAL PROPERTY

All IP generated has been included in related work. (see SAND 2006-6534 and report for project # 93518)

10 CONTACTS:

Greg Nielson: resonant gyroscope
Uma Krishnamoorthy: accelerometers
Mial Warren: accelerometers
J. Mark Harris: accelerometers
William Cowan: nano-photonics gratings for optical filter applications

Distribution

1	MS0899	Technical Library	9536 (electronic only)
1	MS0123	D. Chavez, LDRD Office	1011 (electronic only)


Sandia National Laboratories